

Integrating hetero-coordinated FeN₄ and NiP₄ single-atomic sites in one system for oxygen reduction/evolution

Xiaoyu Qiu (✉ 07255@njnu.edu.cn)

Nanjing Normal University <https://orcid.org/0000-0001-7952-3346>

Keying Su

Nanjing Normal University

Anzhou Yang

Nanjing Normal University

Yawen Tang

Jiangsu Key Laboratory of New Power Batteries, Jiangsu Collaborative Innovation Center of Biomedical Functional Materials, School of Chemistry and Materials Science, Nanjing Normal University, Nanjing

Article

Keywords:

Posted Date: April 14th, 2022

DOI: <https://doi.org/10.21203/rs.3.rs-1542920/v1>

License:   This work is licensed under a Creative Commons Attribution 4.0 International License.

[Read Full License](#)

Abstract

The intrinsic activity of single-atom catalysts highly relies on their coordination configuration. However, selecting heterogenous ligands with larger electronegativity difference to severally customize the coordination and tune the electronic structure of dual-atom catalysts still remains challenge. Herein, a layer-by-layer separation and anisotropic coordination strategy is designed to perform the hetero-coordinated FeN_4 and NiP_4 sites anchored to the inner and outer surfaces of hollow carbon sphere ($\text{FeN}_4\text{-C-NiP}_4$), revealing a ligand-determined electronic properties of metal sites and their selectivity for oxidative/reductive reaction. Specifically, FeN_4 sites with lower spin and deficient electrons are responsible for oxygen reduction reaction (ORR, $E_{1/2}=0.89$ V), while four rich-electronic P ligands upshift the Ni center towards a higher spin, making the NiP_4 sites more favorable for oxygen evolution reaction (OER, $\eta_{10}=218$ mV_{IR-free}). Thus the $\text{FeN}_4\text{-C-NiP}_4$ could balance the competition between rate-limiting steps of ORR and OER, manifesting a small potential gap of 0.59 V. Moreover, above concept can be extended to achieve hetero-coordinated $\text{CoN}_4\text{-C-NiP}_4$ dual-atom sites, enhancing the activity and selectivity for hydrogen evolution reaction (HER) and OER.

Background

Synchronously oxidative and reductive reactions are generally proceeded in one circulation system for various renewable energy conversion devices. For instance, the discharging and charging processes in Zinc-air battery are driven by reversible **oxygen reduction** reaction (ORR, $\text{O}_2 + 2\text{H}_2\text{O} + 4\text{e}^- \rightarrow 4\text{OH}^-$) and oxygen evolution reaction (OER, $4\text{OH}^- \rightarrow 2\text{H}_2\text{O} + \text{O}_2 + 4\text{e}^-$)¹⁻³. Electrochemical water splitting employs hydrogen evolution reaction (HER) as cathodic-half cell **reductive** reaction and OER as anodic-half cell oxidative reaction⁴. In an effort to guarantee the **output power** and meet the compatibility, fabricating bifunctional electro-catalysts that simultaneously possess high oxidative and reductive activity at wide potential range is essential⁵⁻⁷. Very recently, dual-atom catalysts (DACs) without direct bonding have emerged as a novel frontier as bifunctional electro-catalysts⁸, which combine the intrinsic activity of two atomic sites to break through the limitation of single atom catalysts (SACs)^{9, 10}. In addition, compare to directly bonded dual-atoms pair, DACs with separated **spatial distribution** possess more tunability in geometric structure, metal-metal distance and electronic property, which could broaden the regulation scope for key intermediates adsorption and proton-electron transfer pathway^{11, 12}. More importantly, a relative far metal-metal distance has been proven to form two non-interfering catalytic interfaces, which could simultaneously promote the seemingly incompatible oxidative and reductive reactions in one system¹³.

The intrinsic activity of SACs highly relies on the selection of ligands. Based on the discrepancy in size and electronegativity, ligands determine the local **coordination environment** and electronic structure of metal center¹⁴. In particular, P ligand with larger atom radius and lower electronegativity (2.01) can enhance the local charge density through its 3p lone-pair electrons, thereby tuning the adsorption strength

of oxygen-contained species¹⁵. Meanwhile its unoccupied 3d orbitals could accommodate the valence electrons from metal center, accelerating the electron migrations¹⁶. However, metal center usually prefers to coordinate with large-electronegative N (3.04) and C (2.55) ligands due to the effortless formation of M-N/M-C bonds with shorter **bond length** and stronger **bond energy**, leaving difficulty for achieving pure M-P_x single-atom configuration¹⁷. On above basis, when extending the ligand regulation strategy into DACs domain, it is more challenging to use heterogeneous ligands with larger electronegativity difference to severally customize the electronic structure of two metal centers. This is because in most cases for the synthesis of DACs, two metal precursors are inevitably stabilized by similar organic linkers and underwent co-pyrolysis condition, hindering their selective coordination with different ligands¹⁸.

Herein, based on the layer-by-layer separation strategy and anisotropic coordination capacity of metal ions, we realize the fabrication of hetero-coordinated FeN₄ and NiP₄ atomic sites that successively anchored to inner and outer surfaces of hollow carbon sphere (denoted as Janus-distributed FeN₄-C-NiP₄). X-ray photoelectron spectroscopy (XPS) and X-ray absorption fine structure (XAFS) verify the heterogeneous configurations of Fe-N₄ and Ni-P₄ sites, which are **spatial isolation** with negligible interaction. Compare to N-coordinated FeN₄-C-NiN₄, the FeN₄-C-NiP₄ strengthen the charge polarization and widen the spin density gap, generating higher spin NiP₄ sites with electron accumulation and relatively lower spin FeN₄ sites with electron deficiency. By employing mono-component FeN₄, NiP₄, and NiN₄ as references, electrochemical tests and theoretical calculations verify that the FeN₄-C-NiP₄ could provide separated FeN₄ and NiP₄ sites with different selectivity for reversible oxygen catalysis, which responsible for both high ORR and OER activity, small potential gap, and superior charge-discharge performance in Zn-air battery. Particularly, four rich-electronic P ligands upshift the Ni center towards a higher spin to modulate the energy barrier of O* adsorption and optimize the G_{OOH*}-G_{OH*} value to 2.75 eV, which are more favorable for boosting OER than conventional N ligands. Above concept could be extended to perform Janus-distributed CoN₄-C-NiP₄ dual-atom sites, which offer separated CoN₄ and NiP₄ sites to enhance the activity and selectivity for HER and OER, further verifying the role of heterogeneous ligands for oxidative/reductive catalysis.

Results

Synthesis and structural features of hetero-coordinated FeN₄-C-NiP₄. The synthetic route of FeN₄-C-NiP₄ is schematic illustrated in Fig. 1a (SEM images and color change of intermediates shown in Supplementary Fig. 1 and Fig. 2), which involves four steps. Step I: forming SiO₂⁻@Fe³⁺ spheres. SiO₂ nanospheres (150 nm) were pre-synthesized and underwent surface modification to be negatively charged. Then Fe³⁺ were readily adsorbed on SiO₂⁻ to form the SiO₂⁻@Fe³⁺ spheres through electrostatic attractions, accompanied by color change from white to dark orange. Step II: adding excess adenosine monophosphate (AMP⁺) to wrap on the outer surface of SiO₂⁻@Fe³⁺. AMP⁺ molecule was consisted of phosphate functional group, pentose nucleo-saccharide and nitrogenous base adenine, as structure

shown in Supplementary Fig. 3). Selecting cheap and sustainable biomaterial of AMP⁺ as N, P, and C source was due to following three reasons: i) -NH₂ from APM⁺ could provide lone pairs of electrons to strongly bind with Fe³⁺ via coordination interactions, as confirmed by color change and UV-vis in Supplementary Fig. 4. The resultant Fe³⁺-AMP⁺ complex tended to form atomic Fe sites after pyrolysis through spatial confinement effect; ii) AMP⁺ with large molecular weight could intertwine on the surface of SiO₂⁻@Fe³⁺, forming a thick AMP⁺ layer to avoid the contact of inner Fe³⁺ with other metal precursors in subsequent steps. As confirmed by TEM and SEM images in Supplementary Fig. 5, it indicates the completely coverage of AMP⁺ layer with thickness of 25.0 nm on the outer surface of SiO₂⁻@Fe³⁺; iii) the AMP⁺ was positively charged under isoelectric point, beneficial for further electrostatic adsorption. Step III: forming SiO₂⁻@Fe³⁺@AMP⁺@Ni(CN)₄²⁻ spheres. The electronegative [Ni(CN)₄]²⁻ could further adsorb on the outer surface of SiO₂⁻@Fe³⁺@AMP⁺. Specifically, the cyano groups in Ni(CN)₄²⁻ could disperse the central Ni²⁺ to avoid the aggregation after pyrolysis¹⁹. The precise element distribution of SiO₂⁻@Fe³⁺@AMP⁺@Ni(CN)₄²⁻ spheres was examined by EDX mapping (Supplementary Fig. 6), which verifies Janus-like structure consisted of inner Fe³⁺ and outer [Ni(CN)₄]²⁻. Step IIII: pyrolysis and leaching to acquire FeN₄-C-NiP₄. The SiO₂⁻@Fe³⁺@AMP⁺@Ni(CN)₄²⁻ powder was carbothermally reduced to form SiO₂@FeN₄-C-NiP₄ due to anisotropic coordination capacity of Fe³⁺ and Ni²⁺. After pyrolysis, AMP⁺ layer was transformed into N, P-doped carbon spheres, meanwhile the inner Fe³⁺-AMP⁺ and outer AMP⁺-Ni(CN)₄²⁻ were transformed into atomic Fe-N_x sites and Ni-P_x sites, respectively. Particularly, the post transition metal Ni²⁺, which contains much d-orbital electrons and exerts lower charge, preferred to form the Ni-P bonds because the unoccupied 3d orbitals of P could share the electrons pair of Ni²⁺ to form extra back donating bonds²⁰. The increase of bonding number leads to preferential formation of Ni-P than Ni-N. Finally, after leaching to remove the SiO₂, Janus-distributed and hetero-coordinated FeN₄-C-NiP₄ could be yielding.

The FeN₄-C-NiP₄ dual-atom sites were first investigated by X-ray diffraction (XRD) and Raman spectra. The XRD pattern exhibits two broad peaks at 25.7° and 44°, assigned to the (002) and (100) planes of graphitic carbon (Fig. 1b). No diffraction peak ascribed to Fe or Ni could be detected, demonstrating the absence of crystalline Fe and Ni-based species. The Raman spectra shows defects-related D band at 1325 cm⁻¹ and sp²-hybridized carbon-related G band at 1590 cm⁻¹ (Supplementary Fig. 7). The relative high I_D/I_G value (1.11) for FeN₄-C-NiP₄ reveals the defective structure of carbon after pyrolysis. The morphology of FeN₄-C-NiP₄ was investigated by large-scale HRTEM images (Supplementary Fig. 8) and high angle annular dark field scanning TEM (HAADF-STEM, Fig. 1c). Large number of interconnected and hollow nanospheres with diameter of 150 nm and wall thickness of 3.8 nm could be observed, manifesting the structural robustness. Meanwhile, no visible nanoparticles or clusters could be observed, implying the atomic dispersion of both Fe and Ni. The Brunauer-Emmett-Teller surface area of FeN₄-C-NiP₄ was calculated to be 290.71 m² g⁻¹, with a hysteresis loop related to type-IV isotherm (Supplementary Fig. 9), indicative a high specific surface area with mesoporous characteristics. The

mono-dispersion of both Fe and Ni atoms was directly monitored by HAADF-STEM (Fig. 1d). A number of bright dots with size of 2.0 Å are randomly dispersed, corroborating that both Fe and Ni atoms are isolated without the formation of Fe-Ni dual-atom pairs. The energy-dispersive X-ray (EDX) mapping reveals the co-existence of Fe, Ni, C, N, and P elements over the entire architecture (Fig. 1e), confirming the successful doping of P and well reservation of Fe and Ni sites. Inductively coupled plasma atomic emission spectroscopy (ICP-AES) indicates that the weight fraction of Fe and Ni in FeN₄-C-NiP₄ is 1.10 at% and 1.05 at%, respectively.

The valence states and chemical environment of FeN₄-C-NiP₄ were elucidated by XPS (Supplementary Fig. 10). The wide-scan spectrum displays obvious signals of Fe, Ni, C, N, and P (content: 4.64 at%) in FeN₄-C-NiP₄. The high-resolution Fe 2p and Ni 2p spectra show main peaks for Fe²⁺ (709.8 and 723.1 eV), Fe³⁺ (715.2 and 728.9 eV) and Ni²⁺ (854.9 and 872.6 eV), respectively, manifesting the high-valence state of Fe and Ni in FeN₄-C-NiP₄. Theoretically, when electronic effect is existed between Fe and Ni, the Ni atoms could donate partial electrons to Fe atoms, leading to the positive shift of Ni region and correspondingly negative shift of Fe²⁺. Importantly, the FeN₄-C-NiP₄ demonstrate standard location of Fe²⁺/Fe³⁺ and negative shift of Ni²⁺, suggesting a non-existent interaction between Fe and Ni. This is possibly due to a relative far distance between Fe and Ni sites, providing evidence for the spatially separated location of Fe and Ni sites in FeN₄-C-NiP₄. The N 1s spectrum reveals the coexistence of pyridinic N (398.1 eV, 36.8%), pyrrolic N (399.4 eV, 32.4%), and graphitic N (400.6 eV, 30.8%). The P 2p spectra could be fitted into three peaks at 131.9 eV (P 2p_{3/2} for M-P), 132.9 eV (P-C), and 133.8 eV (P-O), respectively. The obvious M-P signal implies the direct bonding between metal and P atoms.

In order to further confirm the Ni-P bond in FeN₄-C-NiP₄, the Ni₂P-doped C nanosheets and mono-component NiN₄ single-atoms were fabricated. Importantly, through directly calcining the mixture of K₂[Ni(CN)₄] and AMP powders, keeping the same ratio used for FeN₄-C-NiP₄, Ni₂P-doped C nanosheets with high purity could be obtained, indicating the strong binding ability between Ni and P (structural features confirmed by HRTEM, XRD, and XPS in Supplementary Fig. 11). Particularly, both the XPS Ni 2p and P 2p spectra for Ni₂P-doped C nanosheets show similar location with those for FeN₄-C-NiP₄, providing evidence for the possible Ni-P bonding in FeN₄-C-NiP₄. Furthermore, mono-component NiN₄ with pure N coordination were synthesized according to previous work²², using the histidine to eliminate the P source. The formation of NiN₄ was confirmed by XRD, HRTEM, HAADF-STEM, EDX mappings, and XPS, as displayed in Supplementary Fig. 12. Supplementary Fig. 13 compares the XPS Ni 2p_{3/2} spectra for FeN₄-C-NiP₄, Ni₂P-doped C nanosheets, and NiN₄. Obviously, the Ni 2p_{3/2} peak of FeN₄-C-NiP₄ and Ni₂P-doped C nanosheets show a negative shift of 0.8 eV than that of the NiN₄, implying non-formation of Ni-N bond in FeN₄-C-NiP₄. Due to the weaker electronegativity of P (2.01) than N (3.04), the charges of Ni adjacent to P atom are less positive, resulting in more negative location of Ni-P than Ni-N.

Atomic structure analysis. XAFS analysis were conducted to decipher the coordination configuration of FeN₄-C-NiP₄ at atomic scale (Supplementary Fig. 14). The pre-edge peak for Fe K edge is situated near

the Fe_2O_3 and shifts to higher energy region than Fe foil and Fe_2P , indicating that the Fe valence in $\text{FeN}_4\text{-C-NiP}_4$ is near + 3 (Fig. 2a). The pre-edge peak for Ni K-edge is located between Ni_2P and NiO , demonstrating the average oxidation state of Ni in $\text{FeN}_4\text{-C-NiP}_4$ is between + 1 and + 2 (Fig. 2b). It is worth noting that the wide-range line-type of Fe K-edge for $\text{FeN}_4\text{-C-NiP}_4$ is similar to that of the Fe_2O_3 with a salient peak at 7132 eV, while the line-type of Ni K-edge for $\text{FeN}_4\text{-C-NiP}_4$ is similar to that of the Ni_2P with mild ridge type. This suggests that the Fe and Ni for $\text{FeN}_4\text{-C-NiP}_4$ might possess similar coordination with Fe_2O_3 and Ni_2P , respectively. The Fourier transform (FT) EXAFS spectra of Fe K-edge and Ni K-edge for $\text{FeN}_4\text{-C-NiP}_4$ are illustrated in Fig. 2c (fitting details shown in Supplementary Figs. 15 and 16). For Fe moiety, the predominant peak located at 1.41 Å is assigned to the backscattering of Fe-N in the first shell, meanwhile no related peak corresponding to Fe-Fe, Fe-P, or Fe-Ni could be detected. For Ni moiety, the sole peak located at 1.81 Å is attributed to the scattering of Ni-P first-shell coordination, which is consisting with the location of Ni-P bonds for Ni_2P . Meanwhile, no Ni-Ni, Ni-N, or Ni-Fe contribution could be observed, confirming the entirely Ni-P bonding in $\text{FeN}_4\text{-C-NiP}_4$. EXAFS wavelet transform (WT) analysis present single intensity maximum at 3.5 \AA^{-1} for Fe K-edge and 5.4 \AA^{-1} for Ni K-edge, respectively (Supplementary Fig. 17). These could be assigned to the Fe-N and Ni-P path, further verifying the isolated feature of FeN_4 and NiP_4 in $\text{FeN}_4\text{-C-NiP}_4$. Quantitatively, the coordination numbers of Fe-N and Ni-P were extracted by EXAFS fitting. Due to the relative large difference in bond length, the coordination parameters of M-N and M-P could be well distinguished. As listed in Supplementary Tables 1 and 2, the coordination numbers for Fe-N were calculated to be 4.3 with bond length of $2.02 \pm 0.01 \text{ \AA}$. The coordination numbers for Ni-P were calculated to be 3.8 with a much longer bond length of $2.25 \pm 0.02 \text{ \AA}$. Thus the hetero-coordinated $\text{Fe}_1\text{-N}_4$ and $\text{Ni}_1\text{-P}_4$ configuration are determined to be the dominating structural motifs.

In order to investigate the role of ligands on tuning the electronic structure, the charge and spin density distribution, and projected density of states (PDOS) of $\text{FeN}_4\text{-C-NiP}_4$ were analyzed by DFT calculations, in comparison with N-coordinated $\text{FeN}_4\text{-C-NiN}_4$. Since the XPS and EXAFS verify negligible interaction between FeN_4 and NiP_4 sites, a relatively far Fe-Ni distance was simulated to avoid the interference. As shown in Fig. 2d, the charge density distribution of FeN_4 and NiN_4 sites for $\text{FeN}_4\text{-C-NiN}_4$ show similar intensity and scope due to the same N coordination. While introducing four P ligands to Ni center, the charge distribution scope of NiP_4 is largely pronounced with increased electron density around Ni center, resulting in electron-rich feature of NiP_4 sites. Comparatively, the FeN_4 sites is electron-deficient with depressed charge distribution. Thus the combination of FeN_4 and NiP_4 sites for $\text{FeN}_4\text{-C-NiP}_4$ shows an obviously enhanced surface charge polarization than N-coordinated $\text{FeN}_4\text{-C-NiN}_4$. Similarly, the spin gap in $\text{FeN}_4\text{-C-NiP}_4$ also becomes wider in comparison with $\text{FeN}_4\text{-C-NiN}_4$. As shown in Fig. 2e, the NiN_4 indicates a higher spin state (0.12) compare to that of the FeN_4 (-0.09). While introducing four P ligands into Ni center, the maximum spin density of NiP_4 further uplifts to 0.19, due to the contribution of 3p lone-pair electrons from P. As a result, the $\text{FeN}_4\text{-C-NiP}_4$ possess higher spin NiP_4 sites and relatively lower spin FeN_4 sites, illustrating that the heterogeneous coordination could further enlarge the spin difference of

dual-metal sites. Moreover, the d band center of FeN₄ and NiP₄ sites in FeN₄-C-NiP₄ exhibit a larger difference in comparison with those in FeN₄-C-NiN₄. As shown in Fig. 2f, the PDOS location follows the order of FeN₄ (-0.208 eV) > NiN₄ (-1.956 eV) > NiP₄ (-2.951 eV). The FeN₄ with electron-deficient feature is endowed with an up-shifted d band center that closer to the Fermi level, while the d band center of NiP₄ is much lower than NiN₄, which is far away from Fermi level. This indicates the P ligands could further downshift the d band center of Ni center, resulting in enlarged difference in d band center of FeN₄ and NiP₄ sites for FeN₄-C-NiP₄. Overall, above results demonstrate the asymmetrical charge, spin, and PDOS deployment in FeN₄-C-NiP₄, which could simultaneously provide two atomic sites with electron accumulation and deficiency, or two atomic sites with high and low spin, as well as two atomic sites with close and far d band center towards Fermi level. Since these electronic properties are closely related to the adsorption behavior of oxygen-contained intermediates and thus determine the intrinsic activity of metal center^{23,24}, the hetero-coordinated FeN₄-C-NiP₄ with stronger charge polarization, wider spin gap, and larger PDOS difference is promising for enlarging the difference in catalytic activity of atomic Fe and Ni sites.

Experimental and theoretical oxygen catalytic mechanism on of FeN₄-C-NiP₄. Since the MN₄-C moiety has been affirmed to follow the activity order of Fe > Co > Ni for ORR, Ni > Co > Fe for OER, and Co > Ni > Fe for HER in alkaline medium²⁵⁻²⁸, the FeN₄-C-NiP₄ dual-atom sites were applied to bifunctional ORR and OER in 0.1 M KOH. To identify the role of separated FeN₄ and NiP₄ sites and shed lights on the hetero-coordination for enhancing electro-catalytic selectivity, mono-component FeN₄, NiP₄, and NiN₄ were employed as references (structural details shown in Supplementary Figs. 18, 19, 12, respectively). The FeNi/Ni₂P nanoparticles synthesized without using SiO₂ template (Supplementary Fig. 20) and hollow C spheres without any metal doping were also used for comparison. As the linear sweep voltammetry (LSV) curves in Fig. 3a, the FeN₄-C-NiP₄ display similar onset potential ($E_{\text{onset}}=1.02$ V) and half-wave potential ($E_{1/2}=0.89$ V) compare to those of the FeN₄ (1.01, 0.89 V), which are much better than those of Pt/C (0.95, 0.83 V) and NiP₄ (0.85, 0.72 V). At 0.9 V, the FeN₄-C-NiP₄ exhibit the j_k of 1.44 mA cm⁻², which is similar to that of the FeN₄ (1.53 mA cm⁻²) and much better than Pt/C and NiP₄ (Fig. 3b). The trend of Tafel slope is consistent with activity, that the FeN₄-C-NiP₄ and FeN₄ show faster ORR kinetics than Pt/C and NiP₄ (Supplementary Fig. 21a). Besides ORR, the FeN₄-C-NiP₄ also present outstanding OER activity, while the activity trend of reference samples are reversed. As shown in Fig. 3c, to reach a current density of 10 mA cm⁻², FeN₄-C-NiP₄ require an overpotential (η) of 247 mV, which is slightly higher than NiP₄ (218 mV) and much lower than NiN₄ (313 mV), RuO₂ (350 mV), and FeN₄ (406 mV). At $\eta = 300$ mV, the FeN₄-C-NiP₄ reach a current density of 53.29 mA cm⁻², which is similar to that of the NiP₄ (49.24 mA cm⁻²) and much higher than the other samples (Fig. 3d). The trend of Tafel slope is consistent with activity, that the FeN₄-C-NiP₄ and NiP₄ show much lower Tafel slope than NiN₄, RuO₂, and FeN₄, revealing the fast OER kinetics over FeN₄-C-NiP₄ and NiP₄ (Supplementary Fig. 21b). In addition, the hollow C spheres without any metal doping exhibit feeble activity for both ORR and OER, as shown in Supplementary Fig. 22. This illustrates

that the hollow carbon spheres in FeN₄-C-NiP₄ are inactive for ORR and OER, verifying the pivotal role of Fe-N₄ and Ni-P₄ as active sites. The FeNi/Ni₂P nanoparticles synthesized without using SiO₂ template exhibit obviously degenerative activity for ORR and OER, in comparison with FeN₄-C-NiP₄ (Supplementary Fig. 23). This verifies the importance of atomic metal sites for enhancing the ORR and OER activity.

Overall, the ORR activity follows the order of FeN₄-C-NiP₄ ≈ FeN₄ > Pt/C > FeNi/Ni₂P > NiP₄ > hollow C spheres, while the OER activity follows the order of NiP₄ ≈ FeN₄-C-NiP₄ > FeNi/Ni₂P > NiN₄ > RuO₂ > FeN₄ > hollow C spheres. Accordingly, following conclusions could be deduced: i) the mono-component FeN₄ sites are highly active for ORR but poor for OER, meanwhile the mono-component NiP₄ sites are highly active for OER but poor for ORR. This illustrates that the FeN₄-C-NiP₄ could provide highly active FeN₄ and NiP₄ sites for ORR and OER, respectively; ii) the ORR activity of FeN₄-C-NiP₄ and FeN₄ is similar, so as the OER activity of FeN₄-C-NiP₄ and NiP₄. This illustrates no obviously synergistic effect is existed between FeN₄ and NiP₄ sites, which is possibly due to a relative far metal-metal distance; iii) the OER activity of NiP₄ atomic sites are much better than NiN₄ atomic sites, testifying the prominent role of four P ligands for promoting OER than conventional N coordination.

Inspired by the high ORR and OER activity, the FeN₄-C-NiP₄ exhibit a small potential gap of 0.59 V, surpassing most of the state-of-art bifunctional catalysts (Supplementary Fig. 24 and Fig. 3e). The ORR and OER stability of FeN₄-C-NiP₄ were evaluated by accelerated durability tests (ADTs) and chronoamperometry (Fig. 3f). The FeN₄-C-NiP₄ dual-atom sites manifest a remarkable long-term stability with negligible decay of $E_{1/2}$ (5 mV) for ORR and $\eta_{10 \text{ mA cm}^{-2}}$ (8 mV) for OER after 5,000 cycles. Chronoamperometry also confirms the durability of FeN₄-C-NiP₄, exhibiting a small degradation of 3.4% and 5.8% after 18,000 s for ORR and OER, respectively. The practicability of FeN₄-C-NiP₄ as bifunctional catalysts was examined by Zn-air battery (Fig. 3g and Supplementary Fig. 25). The FeN₄-C-NiP₄-assembled Zn-air battery could drive the LED light array for more than 24 h and exhibit a small charge-discharge voltage gap (1.18 V@10 mA cm⁻²). After 600 cycles (~ 200 h), it shows up an even better voltage gap to 1.02 V, outperforming the Pt/C + RuO₂ air-cathode (Supplementary Fig. 26).

DFT calculations were carried out to explain the origin of high ORR and OER activity on FeN₄-C-NiP₄ and unravel the explicit role of hetero-coordination. Figure 4a shows the DFT-optimized adsorption configuration of reaction adsorbates on FeN₄ and NiP₄ sites. The adsorption of O₂* is stronger at FeN₄ sites with bonding length of 2.337 Å, which is much shorter than NiP₄ sites (2.539 Å). On the contrary, the adsorption of OH* is stronger at NiP₄ sites with bonding length of 1.901 Å, which is shorter than FeN₄ sites (1.947 Å). These declare that the FeN₄-C-NiP₄ dual-atom sites possess two metal centers with contrasting adsorption behavior. Figure 4b displays the Gibbs free energy profiles on FeN₄ and NiP₄ sites, in an effort to identify the main active sites in FeN₄-C-NiP₄ that determine the ORR and OER, respectively. From left to right, the FeN₄ sites have more significantly exothermic proton-electron transfer steps than NiP₄ sites, indicating a favorable ORR pathway at FeN₄ sites. Moreover, the FeN₄ sites show a more

favorable protonation of O_2^* ($\Delta G_{O_2^* \rightarrow OOH^*} = -0.82$ eV) than NiP_4 (-0.59 eV), further authenticating a faster ORR kinetics on FeN_4 sites. For OER, the free energy difference between G_{OOH^*} and G_{OH^*} ($\Delta G_{OOH^* \rightarrow OH^*}$) is found to be a key reaction descriptor, with the ideal value of 2.46 eV²⁹. The value of $G_{OOH^*} - G_{OH^*}$ for NiP_4 sites (2.75 eV) is closer to 2.46 eV than that of FeN_4 sites (3.16 eV), indicating a favorable OER pathway at NiP_4 sites. Overall, above results suggest the oxygen catalytic selectivity of separated FeN_4 and NiP_4 sites in FeN_4 -C- NiP_4 , which are highly active for ORR and OER, respectively, thus their combination could balance the competition between rate-limiting steps of oxygen reduction/evolution, responsible for both high ORR and OER activity.

To shed lights on the role of hetero-coordination for enhancing the catalytic selectivity of atomic Fe and Ni sites, the ORR pathway at FeN_4 and FeP_4 sites (Fig. 4c and Supplementary Fig. 27), and OER pathway at NiN_4 and NiP_4 sites (Fig. 4d and Supplementary Fig. 28) were compared. For ORR, the FeN_4 and FeP_4 sites show very similar proton-electron transfer pathways, suggesting that for Fe center, selecting four N or four P coordination cause unobvious effect for promoting ORR. On the contrary, for OER, the NiP_4 and NiN_4 sites show disparate proton-electron transfer steps, wherein the first three electron-transfer steps at NiN_4 sites are too fast. As a result, the $\Delta G_{OOH^* \rightarrow OH^*}$ for NiN_4 (3.13 eV) is much far away from 2.46 eV than NiP_4 (2.75 eV). This verifies that for Ni center, four P coordination are more favorable for optimizing OER pathway than N coordination. Combining with the electronic properties illustrated in Fig. 2d-f, the correlation between ligands, electronic structure and oxygen reduction/evolution activity could be clarified. The PDOS is used to explain the improved ORR activity experimentally observed in FeN_4 , as shown in Fig. 4e. According to the d band center theory, a closer d-band center to the Fermi level represents a strong binding ability for surface adsorbed O_2^* species^{30, 31}. Accordingly, the electron-deficient FeN_4 sites with up-shifted d-band center are more favorable for adsorbing O_2^* as reactant and possess a faster O_2^* protonation pathway (as evidenced by the short O_2^* bonding length of 2.337 Å and $\Delta G_{O_2^* \rightarrow OOH^*} = -0.82$ eV) compare to both NiN_4 and NiP_4 sites, resulting in higher ORR activity. The spin density is served to explain the strongly enhanced OER activity experimentally observed in NiP_4 , as shown in Fig. 4f. For OER, the $\Delta G_{OOH^* \rightarrow OH^*}$ is largely restricted by the stability of O^* adsorption, that either too strong or too weak O^* adsorption leads to an increase in $\Delta G_{OOH^* \rightarrow OH^*}$ ³². Significantly, the high spin NiP_4 sites could stabilize the unpaired electron of O^* through the exchange interactions, balancing the too fast and too slow transformation to OOH^* at NiN_4 and FeN_4 sites, respectively, resulting in an ideal $\Delta G_{OOH^* \rightarrow OH^*}$ of 2.75 eV and thus responsible for the outstanding OER activity. Overall, above results indicate the role of heterogeneous N, P coordination for respectively customizing the electronic structure of atomic Fe and Ni sites and thus enhancing the selectivity for oxygen catalytic reaction than conventional N coordination. Specifically, the FeN_4 sites with closer d-band center towards the Fermi level are responsible for ORR, while the NiP_4 sites with higher spin are more favorable for OER than both FeN_4 and NiN_4 sites, as schematic shown in Fig. 4g.

Generality of the synthesis of hetero-coordinated dual-atom sites. Above concept of using heterogeneous ligands to severally customize the electronic structure of dual atom sites could be extended to perform Janus-distributed $\text{CoN}_4\text{-C-NiP}_4$. The structural features was confirmed by HADDF-STEM image (Fig. 5a-b), EDX-mapping (Fig. 5c), HRTEM, XRD, and XPS analysis (Supplementary Figs. 29, 30). The dominated active sites for HER and OER in $\text{CoN}_4\text{-C-NiP}_4$ were first analyzed by DFT calculations (Fig. 5d). The free energy of hydrogen adsorption at CoN_4 is as low as 0.07 eV, which is much closer to 0 eV than that of the NiP_4 (1.35 eV), indicating more favorable HER kinetics at CoN_4 sites. The other side, the Gibbs free energy profiles for OER show a smaller $\Delta G_{\text{OOH}^*-\text{OH}^*}$ value and a faster proton-electron transfer pathway at NiP_4 sites, in comparison with CoN_4 sites, suggesting a more favorable OER kinetics at NiP_4 sites. Thus the combination of separated CoN_4 and NiP_4 sites in $\text{CoN}_4\text{-C-NiP}_4$ is theoretically promising for generating high HER and OER activity, simultaneously. The experimental HER and OER performance of $\text{CoN}_4\text{-C-NiP}_4$ were examined by polarization curves obtained in 0.1 M KOH (Fig. 5e-f), and the trends were summarized in Fig. 5g. The $\eta_{10 \text{ mA cm}^{-2}}$ for HER follows the order of Pt/C (96 mV) > $\text{CoN}_4\text{-C-NiP}_4$ (117 mV) \approx CoN_4 (124 mV) > NiP_4 (249 mV). Meanwhile the $\eta_{10 \text{ mA cm}^{-2}}$ for OER follows the order of $\text{CoN}_4\text{-C-NiP}_4$ (206 mV) \approx NiP_4 (218 mV) > RuO_2 (350 mV) > CoN_4 (370 mV). These experimentally confirm that the separated CoN_4 and NiP_4 sites in $\text{CoN}_4\text{-C-NiP}_4$ possess different selectivity for HER and OER, well consistent with the DFT calculation. As a result, the $\text{CoN}_4\text{-C-NiP}_4$ dual-atom sites achieve a small voltage difference of 1.53 V to reach 10 mA cm^{-2} (Supplementary Fig. 31), surpassing most of the state-of-art non-precious bifunctional catalysts (Supplementary Table 4). The practicability of $\text{CoN}_4\text{-C-NiP}_4$ was evaluated by applied to bifunctional electrodes for water splitting. As shown in Fig. 5h, the $\text{CoN}_4\text{-C-NiP}_4$ electrodes require a cell potential of 1.544 V to afford 10 mA cm^{-2} , which is even equal to that of the Pt/C// RuO_2 , as well as exhibit a long-range stability operated for 24 h (Supplementary Fig. 32).

Discussion

In summary, we realize the integration of two **spatial**-separated atomic sites in one system and select heterogeneous ligands to severally regulate their **electronic structure**, aiming at simultaneously achieving high oxidative and reductive activity. Through layer-by-layer electrostatic absorption, space-confinement pyrolysis and anisotropic coordination, Janus-distributed $\text{FeN}_4\text{-C-NiP}_4$ (or $\text{CoN}_4\text{-C-NiP}_4$) with hetero-coordination could be fabricated. The heterogeneous N, P coordination enlarges the difference in **electronic structure** of atomic Fe and Ni sites, generating higher spin NiP_4 with electron accumulation but lower spin FeN_4 with electron deficiency, providing an ideal model to systematically study the structure-function relationship towards oxidative/reductive reaction. Electrochemical tests and DFT calculation verify that the FeN_4 sites with upshifted d-band center are dominated active sites for ORR, while the NiP_4 sites with higher spin are more active for OER, enabling $\text{FeN}_4\text{-C-NiP}_4$ to balance the competition between rate-limiting steps of ORR and OER. This work realizes the heterogeneous ligands design on dual metal sites, which opens an avenue for simultaneously catalyzing various complex oxidative/reductive reactions in one system.

Declarations

Acknowledgements

X.Q. acknowledges the financial supports from National Natural Science Foundation of China (21902078). Y.T. acknowledges the financial supports from National Natural Science Foundation of China (21875112). We also acknowledge the supports from National and Local Joint Engineering Research Centre of Biomedical Functional Materials and a project sponsored by the Priority Academic Program Development of Jiangsu Higher Education Institutions.

Author contributions

X.Q. conceived the idea. X.Q., K.S., and A.Z. performed the experiments. X.Q. and Y.T. analyzed the data and supervised the project. X.Q. wrote the manuscript with contributions from all coauthors. All authors discussed the results.

Competing interests

The authors declare no competing interests.

Additional information

Supplementary information The online version contains supplementary material available at <https://>

Methods

Synthesis of hetero-coordinated $\text{FeN}_4\text{-C-NiP}_4$ and $\text{CoN}_4\text{-C-NiP}_4$. Firstly, SiO_2 nanospheres with a diameter of 150 nm were synthesized via a conventional stöber method³³. Then a layer-by-layer self-assembly approach was served to prepare PSS/PDDA/PSS/PDDA-modified SiO_2 according to our previously study.³⁴ This step could make the SiO_2 to be strongly negative-charged (denoted as SiO_2^-), in an effort to further adsorbing species with positive charges.

For a typical synthesis of Janus-distributed $\text{FeN}_4\text{-C-NiP}_4$, 100 mg of SiO_2^- nanospheres and 160 mg of $\text{Fe}(\text{NO}_3)_3 \cdot 9\text{H}_2\text{O}$ were added into 10 mL of deionized water and ultrasonically dispersed for 10 min. Then the suspension was centrifuged to remove the excess Fe^{3+} in the supernate and the precipitated $\text{SiO}_2^- @\text{Fe}^{3+}$ spheres was picked up and re-dispersed in 10 mL of deionized water for further use. Subsequently, 500 mg of AMP was added into above solution and the pH value was adjusted to 4~5 (lower than [isoelectric point](#)), stirring for 1 h to obtain the $\text{SiO}_2^- @\text{Fe}^{3+} @\text{AMP}^+$ suspension. Then the solution was centrifuged to remove the excess AMP^+ in the supernate and the precipitated $\text{SiO}_2^- @\text{Fe}^{3+} @\text{AMP}^+$ solid was picked up and re-dispersed in 10 mL of deionized water. Afterwards, 80 mg of $\text{K}_2[\text{Ni}(\text{CN})_4]$ was added

into above mixture and stirred for 1 h to form the $\text{SiO}_2^- @ \text{Fe}^{3+} @ \text{AMP}^+ @ [\text{Ni}(\text{CN})_4]^{2-}$. After centrifuge to remove the excess $[\text{Ni}(\text{CN})_4]^{2-}$, vacuum drying, and grinding, the resultant $\text{SiO}_2^- @ \text{Fe}^{3+} @ \text{AMP}^+ @ [\text{Ni}(\text{CN})_4]^{2-}$ powder was placed in a porcelain boat, and calcined at 700 °C under N_2 flow for 3 h (ramp rate: 3 °C min⁻¹) to form the black $\text{SiO}_2 @ \text{FeN}_4\text{-C-NiP}_4$ powder. At last, the products were leached in 10 mL of HF solution (40%) overnight and then washed to neutral to acquire the hetero-coordinated $\text{FeN}_4\text{-C-NiP}_4$ hollow spheres (yielding: ca. 0.358 g).

The synthesis of hetero-coordinated $\text{CoN}_4\text{-C-NiP}_4$ was similar to that of the $\text{FeN}_4\text{-C-NiP}_4$, except for using 200 mg of $\text{Co}(\text{NO}_3)_3 \cdot 9\text{H}_2\text{O}$ to substitute the $\text{Fe}(\text{NO}_3)_3 \cdot 9\text{H}_2\text{O}$.

Synthesis of mono-component FeN_4 , NiP_4 , NiN_4 , and hollow C spheres. A series of mono-component single-atom catalysts were prepared to authenticate the main active sites in $\text{FeN}_4\text{-C-NiP}_4$ and investigate the role of hetero-coordination for bifunctional catalysis. The FeN_4 was synthesized by using the standard procedure of $\text{FeN}_4\text{-C-NiP}_4$ except for without adding $\text{K}_2[\text{Ni}(\text{CN})_4]$, as schematic illustrated in Supplementary Fig. 18. Likewise, the NiP_4 was synthesized by using the standard procedure except for without adding $\text{Fe}(\text{NO}_3)_3 \cdot 9\text{H}_2\text{O}$, as schematic illustrated in Supplementary Fig.19. The synthesis of NiN_4 with pure nitrogen ligands was similar to that of the NiP_4 , except for using the His^+ to substitute AMP^+ , in an effort to eliminate the P source (as shown in Supplementary Fig.12). The C hollow spheres without any metal sites was synthesized by directly coating the AMP^+ onto the surface of SiO_2^- to form the $\text{SiO}_2^- @ \text{AMP}^+$ spheres. Subsequently, the calcining and leaching process was served to obtain the hollow C spheres.

Characterizations. HRTEM were performed on JEOL JEM-2100F transmission electron microscopy. AC-HAADF-STEM images were recorded on JEOL JEM-ARM 200F at an accelerating voltage of 200 k eV. SEM and EDX analysis were performed with a Hitachi S5500 SEM/STEM. XRD were recorded on Rigaku MiniFlex 600 I diffractometer with Cu K α radiation ($\lambda = 1.5406 \text{ \AA}$). ICP-MS was analyzed on Thermo X Series II ICP/MS quadrupole system, Thermo Fisher Scientific. BET surface area was analyzed on Micromeritics ASAP 2050 system at 77 K. Raman spectrum was recorded on Raman spectrometer (LabRAM HR800, $\lambda = 514 \text{ nm}$). UV-*vis* spectra were measured on a Shimadzu UV3600 spectrophotometer at 25 °C equipped with 1.0 cm quartz cells. XPS measurements were conducted on a Thermo VG Scientific ESCALAB 250 spectrometer with an Al K α radiator. The binding energy was calibrated by means of the C 1s peak energy at 284.6 eV. XAFS spectra were measured at the beamline BL14W1 station of the Taiwan Synchrotron Radiation Facility. The obtained XAFS data was processed in Athena (version 0.9.26) for background, pre-edge line and post-edge line calibrations. Then Fourier transformed fitting was carried out in Artemis (version 0.9.26). For Wavelet Transform analysis, the $\chi(k)$ exported from Athena was imported into the Hama Fortran code. The parameters were listed as R range of 1-4 Å , k range of 0-13 Å^{-1} , k weight of 2, and Morlet function with $\kappa = 10$, $\sigma = 1$ was used as the mother wavelet to provide the overall distribution.

Electrochemical measurements. All electrochemical measurements were performed on a CHI 760D electrochemical analyzer (Shanghai Chenhua Co.) by using a standard three electrode system, which consisted of the rotating ring-disk electrode (RRDE) covered with the catalysts as the working electrode (0.196 cm^2), a saturated calomel electrode (SCE) as the reference electrode, and a graphite rod as the auxiliary electrode. All potentials were calibrated into the reversible hydrogen electrode (RHE), using the following equation: $E_{\text{RHE}} = E_{\text{SCE}} + 0.0592 \text{ pH} + 0.242$. The catalyst ink was prepared by ultrasonically dispersing the mixture of 5 mg of catalyst, 0.9 mL ethanol, and 0.1 mL of Nafion (5 wt.%). Then 10 μL of the catalysts was casted on electrode and dried at room temperature. The ORR measurements were performed on the RRDE voltammograms in 0.1 M KOH electrolyte at a rotation rate of 1600 rpm and a scan rate of 5 mV s^{-1} . Before testing, O_2 flow was purged into the electrolyte for at least 30 min to saturate the electrolyte. The OER and HER measurements were evaluated by linear sweep voltammetry (LSV) in N_2 -saturated 0.1 M KOH electrolyte with a scan rate of 5 mV s^{-1} . The linear region of the plots were fitted using the Tafel formula $Z = b \log(j) + a$, where Z referred to overpotential, j referred to current density, and b referred to the Tafel slope.

Zn-air battery and overall water splitting tests. The Zn-air battery tests were performed on a homemade Zn-air cell. The air cathode consisted of a hydrophobic carbon paper with catalyst layer on the electrolyte-facing side and a gas-diffusion layer on the air-facing side. The catalyst ink was dropped and painted onto the carbon paper (1.0 cm^2) to form the catalyst layer with loading of 10 mg cm^{-2} . A well-polished Zn plate with a thickness of 0.3 mm was served as anode and the 0.2 M ZnCl_2 + 6 M KOH solution was used as electrolyte. The cycling stability tests were performed on Land CT2001A system with 5 min rest time between each discharge and charge at a current density of 5 mA cm^{-2} . Each discharge and charge period was set to be 10 min.

The overall water splitting measurements were conducted in a two-electrode system composed of two pieces of nickel foams ($3 \text{ cm} \times 1 \text{ cm}$). The pre-cleaned nickel foams were wrapped with Teflon tape at the $2 \text{ cm} \times 1 \text{ cm}$ area from one end, leaving the rest $1 \text{ cm} \times 1 \text{ cm}$ area exposed for the deposition of catalyst with loading mass of 2 mg cm^{-2} . The overall water splitting tests were performed in 0.1 M KOH electrolyte at a scan rate of 5 mV s^{-1} by using the catalyst-modified nickel foams as cathode and anode, respectively.

Theoretical calculation. The Vienna Ab Initio Package (VASP) was employed to perform all the density functional theory (DFT) calculations within the generalized gradient approximation (GGA) using the PBE formulation. The projected augmented wave (PAW) potentials were served to describe the ionic cores and took valence electrons into account using a plane wave basis set with a kinetic energy cutoff of 400 eV. Partial occupancies of the Kohn-Sham orbitals were allowed using the Gaussian smearing method and a width of 0.05 eV. The electronic energy was considered self-consistent when the energy change was smaller than 10^{-5} eV. A geometry optimization was considered convergent when the force change was smaller than 0.05 eV/\AA . During structural optimizations, the $3 \times 3 \times 1$ Monkhorst-Pack k-point grid for Brillouin zone was used for k-point sampling for structures. The Fe-N_4 and Ni-P_4 structures were modelled

as the Fe single-atom doped at the carbon layer with four N ligands and Ni single-atom doped at the carbon layer with four P ligands. All the atoms were allowed to relax during geometric optimization. The free energy (ΔG) for elemental reaction step were calculated as: $\Delta G = \Delta E + \Delta E_{ZPE} - T\Delta S$, where ΔE is the difference between the total energy, ΔE_{ZPE} and ΔS are the differences in the zero-point energy and the change of entropy, T is the temperature respectively.

References

1. Sun, W. et al. A rechargeable zinc-air battery based on zinc peroxide chemistry. *Science* **371**, 46–51 (2021).
2. Jiang, Y. et al. Linker-compensated metal-organic framework with electron delocalized metal sites for bifunctional oxygen electrocatalysis. *J. Am. Chem. Soc.* **144**, 4783–4791 (2022).
3. Zhou, C. et al. Superdurable bifunctional oxygen electrocatalyst for high-performance zinc-air batteries. *J. Am. Chem. Soc.* **144**, 2694–2704 (2022).
4. Li, M. et al. Exclusive strain effect boosts overall water splitting in PdCu/Ir core/shell nanocrystals. *Angew. Chem. Inter. Ed.* **60**, 8243–8250 (2021).
5. Wang, H. et al. Significantly enhanced overall water splitting performance by partial oxidation of Ir through Au modification in core-shell alloy structure. *J. Am. Chem. Soc.* **143**, 4639–4645 (2021).
6. Yin, K. et al. One nanometer PtIr nanowires as high-efficiency bifunctional catalysts for electrosynthesis of ethanol into high value-added multicarbon compound coupled with hydrogen production. *J. Am. Chem. Soc.* **143**, 10822–10827 (2021).
7. Li, B.Q. et al. Framework-porphyrin-derived single-atom bifunctional oxygen electrocatalysts and their applications in Zn-air batteries. *Adv. Mater.* **31**, 1900592 (2019).
8. Yang, G. et al. Regulating Fe-spin state by atomically dispersed Mn-N in Fe-N-C catalysts with high oxygen reduction activity. *Nat. Commun.* **12**, 1–10 (2021).
9. Han, X. et al. Atomically dispersed binary Co-Ni sites in nitrogen-doped hollow carbon nanocubes for reversible oxygen reduction and evolution. *Adv. Mater.* **31**, 1905622 (2019).
10. Liu, M. et al. A “pre-constrained metal twins” strategy to prepare efficient dual-metal-atom catalysts for cooperative oxygen electrocatalysis. *Adv. Mater.*, 2107421 (2022).
11. Wan, W. et al. Mechanistic insight into the active centers of single/dual-atom Ni/Fe-based oxygen electrocatalysts. *Nat. Commun.* **12**, 1–13 (2021).
12. Bai, L., Hsu, C.-S., Alexander, D.T., Chen, H.M. & Hu, X. A cobalt-iron double-atom catalyst for the oxygen evolution reaction. *J. Am. Chem. Soc.* **141**, 14190–14199 (2019).
13. Zhao, Y. et al. Simultaneous oxidative and reductive reactions in one system by atomic design. *Nat. Catal.* **4**, 134–143 (2021).
14. Long, X. et al. Graphitic phosphorus coordinated single Fe atoms for hydrogenative transformations. *Nat. Commun.* **11**, 1–12 (2020).

15. Zhou, P. et al. Thermolysis of noble metal nanoparticles into electron-rich phosphorus-coordinated noble metal single atoms at low temperature. *Angew. Chem. Inter. Ed.* **58**, 14184–14188 (2019).
16. Yuan, K. et al. Boosting oxygen reduction of single iron active sites via geometric and electronic engineering: nitrogen and phosphorus dual coordination. *J. Am. Chem. Soc.* **142**, 2404–2412 (2020).
17. Chen, Y. et al. Enhanced oxygen reduction with single-atomic-site iron catalysts for a zinc-air battery and hydrogen-air fuel cell. *Nat. Commun.* **9**, 1–12 (2018).
18. Zhao, X., Wang, F., Kong, X.-P., Fang, R. & Li, Y. Dual-metal hetero-single-atoms with different coordination for efficient synergistic catalysis. *J. Am. Chem. Soc.* **143**, 16068–16077 (2021).
19. Chen, J. et al. Dual single-atomic Ni-N₄ and Fe-N₄ sites constructing janus hollow graphene for selective oxygen electrocatalysis. *Adv. Mater.* **32**, 2003134 (2020).
20. Shi, Y., Li, M., Yu, Y. & Zhang, B. Recent advances in nanostructured transition metal phosphides: synthesis and energy-related applications. *Energ. Environ. Sci.* **13**, 4564–4582 (2020).
21. Jiao, L. et al. Non-bonding interaction of neighboring Fe and Ni single-atom pairs on MOF-derived N-doped carbon for enhanced CO₂ electroreduction. *J. Am. Chem. Soc.* **143**, 19417–19424 (2021).
22. Chen, Y. et al. Atomic Fe dispersed on N-doped carbon hollow nanospheres for high-efficiency electrocatalytic oxygen reduction. *Adv. Mater.* **31**, 1806312 (2019).
23. Gao, R. et al. Pd/Fe₂O₃ with electronic coupling single-site Pd-Fe pair sites for low-temperature semihydrogenation of alkynes. *J. Am. Chem. Soc.* **144**, 573–581 (2021).
24. Gao, K. et al. Efficient metal-free electrocatalysts from N-doped carbon nanomaterials: mono-doping and Co-doping. *Adv. Mater.* **31**, 1805121 (2019).
25. Peng, H. et al. Effect of transition metals on the structure and performance of the doped carbon catalysts derived from polyaniline and melamine for ORR application. *ACS Catal.* **4**, 3797–3805 (2014).
26. Wang, X.X. et al. Nitrogen-coordinated single cobalt atom catalysts for oxygen reduction in proton exchange membrane fuel cells. *Adv. Mater.* **30**, 1706758 (2018).
27. Fei, H. et al. General synthesis and definitive structural identification of MN₄C₄ single-atom catalysts with tunable electrocatalytic activities. *Nat. Catal.* **1**, 63–72 (2018).
28. Subbaraman, R. et al. Trends in activity for the water electrolyser reactions on 3d M (Ni, Co, Fe, Mn) hydr (oxy) oxide catalysts. *Nat. Mater.* **11**, 550–557 (2012).
29. Li, H. et al. Oxygen reduction reaction on classically immiscible bimetallics: a case study of RhAu. *J. Phys. Chem. C* **122**, 2712–2716 (2018).
30. Xiao, M. et al. Climbing the apex of the ORR volcano plot via binuclear site construction: electronic and geometric engineering. *J. Am. Chem. Soc.* **141**, 17763–17770 (2019).
31. Chen, Z. et al. Unraveling the origin of sulfur-doped Fe-N-C single-atom catalyst for enhanced oxygen reduction activity: effect of iron spin-state tuning. *Angew. Chem. Inter. Ed.* **133**, 25608–25614 (2021).
32. Li, Z. et al. Tuning the spin density of cobalt single-atom catalysts for efficient oxygen evolution. *ACS Nano* **15**, 7105–7113 (2021).

33. Stöber, W., Fink, A. & Bohn, E. Controlled growth of monodisperse silica spheres in the micron size range. *J. Coll. Inter. Sci.* **26**, 62–69 (1968).
34. Qiu, X. et al. Template-engaged synthesis of hollow porous platinum-palladium alloy nanospheres for efficient methanol electro-oxidation. *J. Power Sources* **302**, 195–201 (2016).

Figures

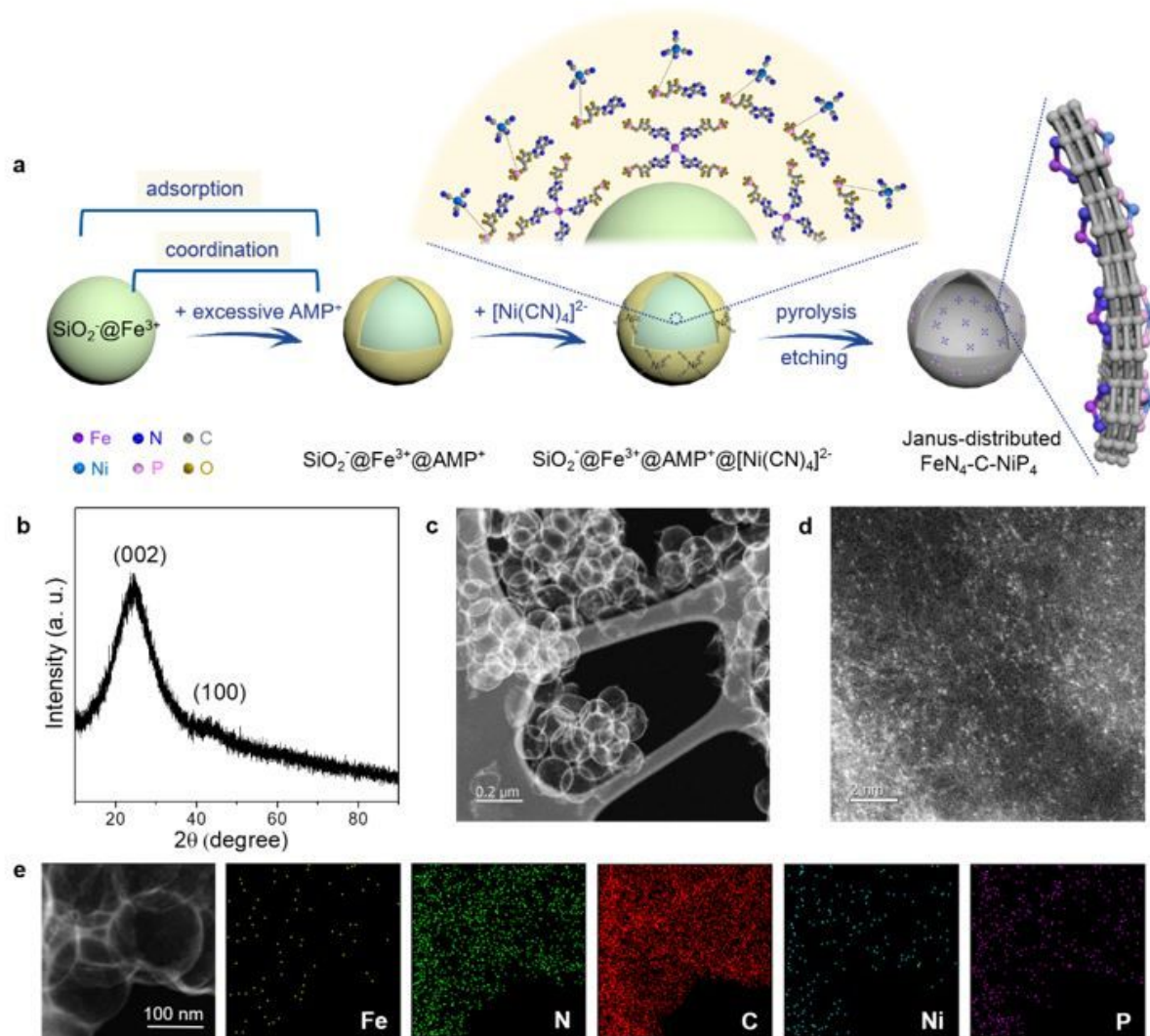


Figure 1

Structural characteristics of Janus-distributed $\text{FeN}_4\text{-C-NiP}_4$. a Schematic illustration. b XRD pattern. c, d HAADF-STEM images. e EDX mappings.

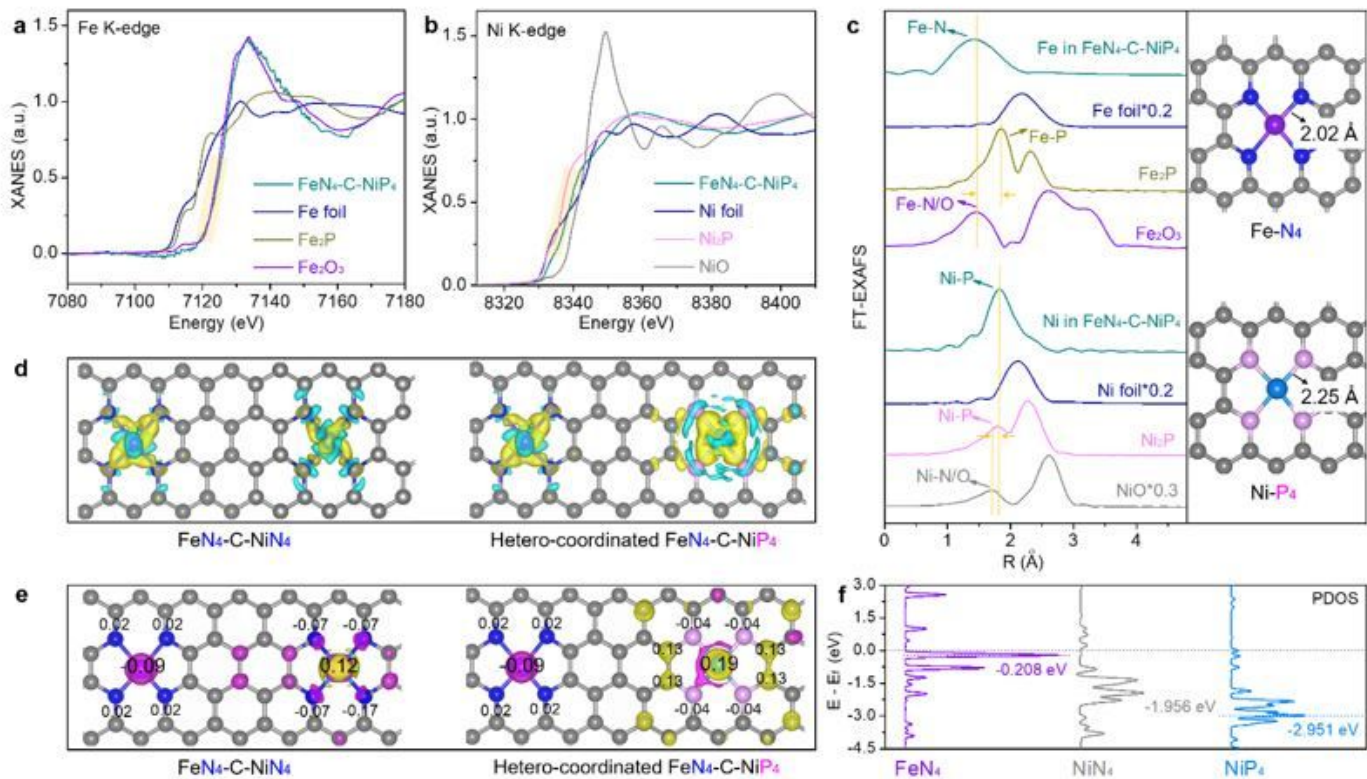


Figure 2

Atomic structure analysis of FeN₄-C-NiP₄. **a** Fe K-edge and **b** Ni K-edge XANES spectra. **c** Fourier transform EXAFS spectra. **d** Differential charge density (blue and yellow represent the charge depletion and accumulation, respectively). **e** Spin density differences (pink and yellow represent spin down and spin up, respectively, the isosurface is $5 \times 10^{-3} e \text{ \AA}^{-3}$). **f** Projected density of states analysis.

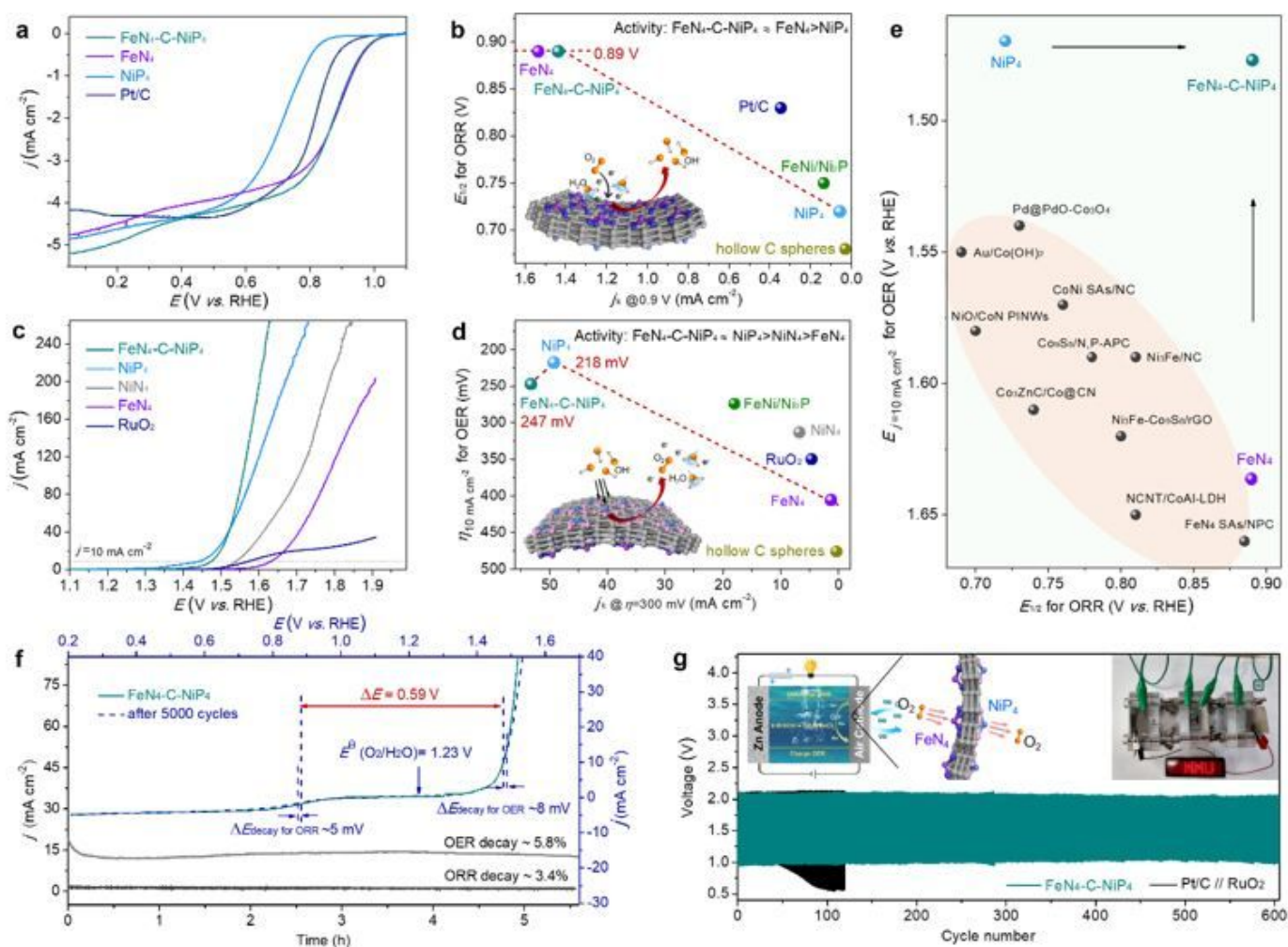


Figure 3

ORR and OER performance of FeNi₄-C-NiP₄ in O₂-saturated 0.1 M KOH. a ORR polarization curves and **b** trend in $E_{1/2}$ and j_k at 0.9 V. **c** OER polarization curves and **d** trend in $\eta_{10 \text{ mA cm}^{-2}}$ and j_k at $\eta = 300 \text{ mV}$. **e** Comparison of $E_{1/2}$ for ORR and $E_{j=10 \text{ mA cm}^{-2}}$ for OER with state-of-art bifunctional catalysts. **f** Overall polarization curve and stability tests, up: ADTs, down: chronoamperometry for OER at 1.55 V and ORR at 0.61 V vs. RHE. **g** Discharge and charge voltage profiles at 5 mA cm^{-2} , insert: schematic diagram of Zn-air battery and LEDs illumination.

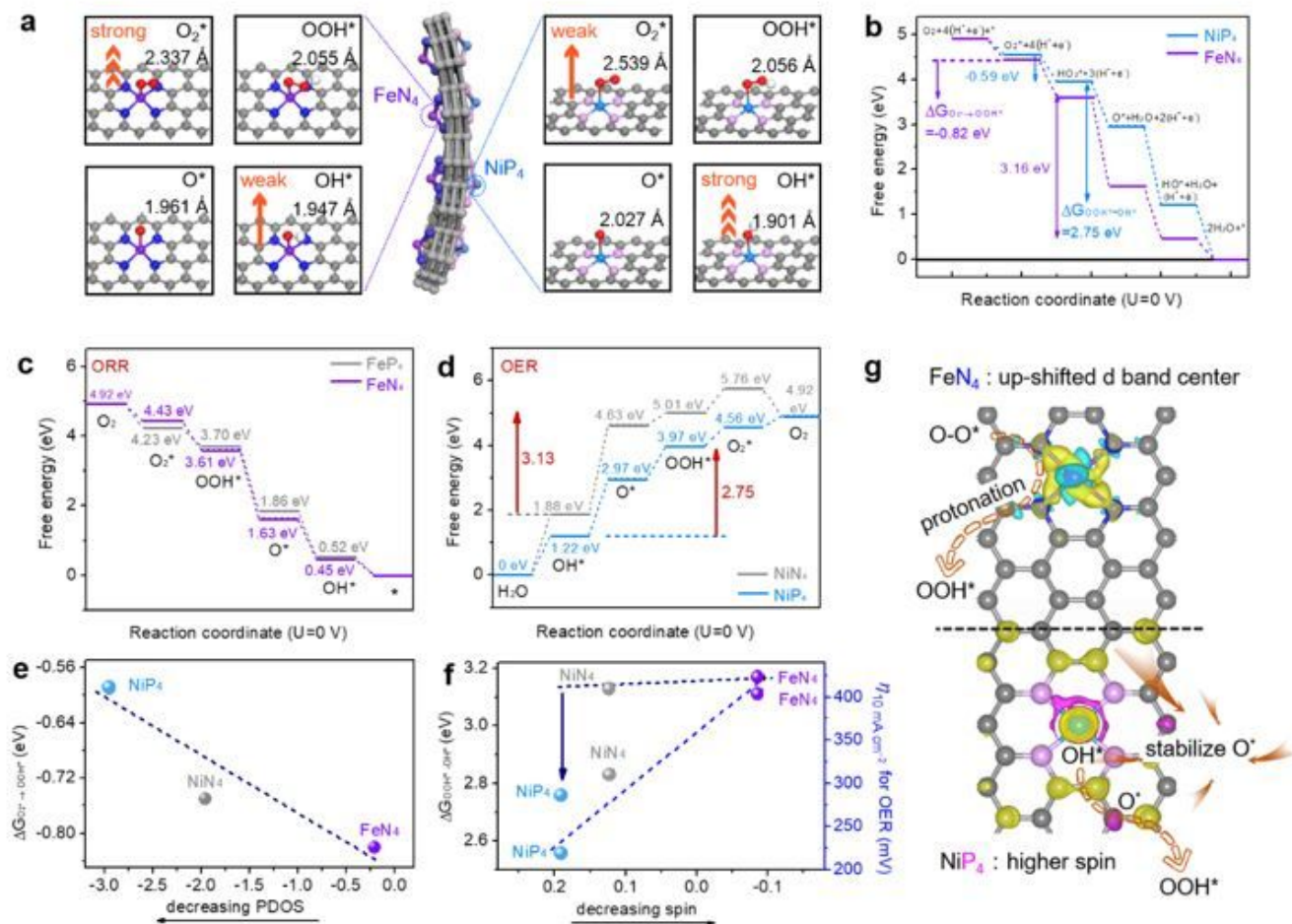


Figure 4

Theoretical analysis of ORR and OER on FeN₄-C-NiP₄. **a** DFT-optimized adsorption configurations of reaction adsorbates and **b** Gibbs free energy profiles on FeNi₄ and NiP₄ (U= 0 V). **c** ORR free energy diagrams on FeN₄ and FeP₄ sites, respectively. **d** OER free energy diagrams on NiP₄ and NiN₄ sites, respectively. **e** Correlation between PDOS and ΔG_{O₂^{*}→OOH^{*}}. **f** Correlation between spin density and ΔG_{OOH^{*}→OH^{*}}. **g** Oxygen catalytic mechanism on FeN₄-C-NiP₄.

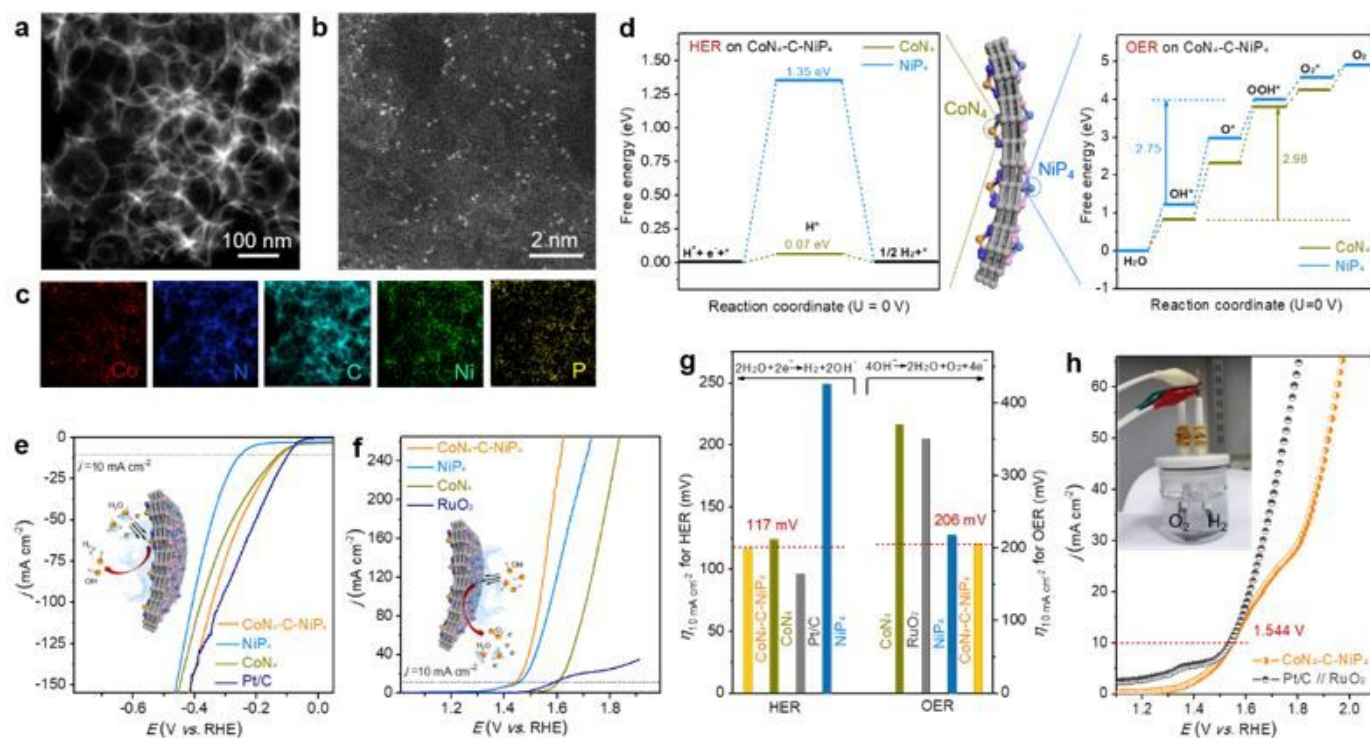


Figure 5

HER and OER mechanism on CoN₄-C-NiP₄. **a, b** HAADF-STEM images. **c** Corresponding EDX mappings. **d** Gibbs free energy profiles. **e** HER and **f** OER polarization curves in O₂-saturated 0.1 M KOH. **g** Trend of overpotentials at 10 mA cm⁻² for HER and OER. **h** Polarization curves for overall water splitting at a scan rate of 2 mV s⁻¹ in 0.1 M KOH.

Supplementary Files

This is a list of supplementary files associated with this preprint. Click to download.

- [SP.docx](#)